LASER & PHOTONICS REVIEWS
www.lpr-journal.org

Silicon Nanomembrane Miniaturized Spectrometer with Wedge-Shaped Structures via CMOS-Compatible Fabrication

*Yuhang Hu, Chunyu You, Zhi Zheng, Binmin Wu, Ziyu Zhang, Chang Liu, Bingxin Chen, Zhiyuan Qiao, Mingze Ma, Tianjun Cai, Xing Li, Yang Wang, Jiachuo He, Changlin Zheng, Xiangzhong Chen, Enming Song, Jizhai Cui, Zhenghua An, Qinglei Guo, Gaoshan Huang, and Yongfeng Mei**

Miniaturized reconstructive spectrometers are of critical significance as they enable the acquisition of incident spectra for analysis with a compact footprint by utilizing reconstruction techniques. However, the typical miniaturized reconstructive spectrometers are not readily adaptable to large-scale production due to their lack of compatibility with complementary metal-oxide-semiconductor (CMOS) manufacturing. Here a silicon nanomembrane miniaturized spectrometer with wedge-shaped structures based on the silicon-on-insulator wafer is demonstrated. The fabrication technique is straightforward and CMOS-compatible, suggesting the potential of wafer-scale manufacturing. The atomic-level thickness variation of the structure enables our spectrometer to theoretically achieve a high level of integration. The spectrometer achieves a resolution of ≈1.85 nm and a spectral wavelength accuracy of up to ≈0.1 nm in a broad bandwidth (from 400 to 1 000 nm) with micron-scale footprint. Furthermore, the spectrometer's spectrum imaging capabilities are also showcased. This research will introduce a feasible paradigm for miniaturized reconstructive spectrometers with a high performance and the potential for commercial application.

1. Introduction

Optical spectrometers are playing an increasingly vital role in multidisciplinary scientific research as well as in industrial production, which have been widely applied in the fields including but not limited to material characterization, industrial inspection, and environmental monitoring.[1–6] Conventional benchtop spectrometers hitherto have been developed to exhibit extraordinary performance with high spectral resolutions and broad working bandwidths. Nevertheless, with an ever-growing demand for the portable, affordable, robust, and energy-efficient devices, consistent progress has been made in miniaturizing spectrometers while retaining appropriate performance in the past few decades.[7,8] Generally, the conventional strategies toward miniaturizing spectrometers can be divided into three categories: i) using customized dispersive optics to split light into different detectors,[9] ii) using narrowband filters to selectively transmit light of specific wavelength to detector,[10,11] iii) employing interferometer to analyze the spectrum by Fourier transform system.[12,13] Those miniaturized spectrometers actually take advantage of the same fundamental principle as that of traditional spectrometers. Nevertheless, the trade-offs between the device performance and the footprint are inevitable in the majority of the situations. For instance, when minimizing the spectrometers toward submillimeter scales, the optical path lengths required to discriminate between wavelengths are affected by the physical size and other factors such as light diffraction, which may prevent the spectrometer from

Y. Hu, C. You, Z. Zheng, Z. Zhang, C. Liu, Z. Qiao, M. Ma, T. Cai, X. Li, Y. Wang, X. Chen, E. Song, J. Cui, G. Huang, Y. Mei
International Institute of Intelligent Nanorobots and Nanosystems
Fudan University
Shanghai 200438, P. R. China
E-mail: yfm@fudan.edu.cn

Y. Hu, C. You, Z. Zheng, Z. Zhang, C. Liu, Z. Qiao, M. Ma, T. Cai, X. Li, Y. Wang, X. Chen, E. Song, J. Cui, G. Huang, Y. Mei
Yiwu Research Institute of Fudan University
Yiwu, Zhejiang 322000, P. R. China

B. Wu
State Key Laboratory of Infrared Physics
Shanghai Institute of Technical Physics
Chinese Academy of Sciences
Shanghai 200083, P. R. China

B. Chen, J. He, C. Zheng, Z. An
State Key Laboratory of Surface Physics &Institute for Nanoelectronic Devices and Quantum Computing
Department of Physics
Fudan University
Shanghai 200438, P. R. China

The ORCID identification number(s) for the author(s) of this article can be found under https://doi.org/10.1002/lpor.202402211

DOI: 10.1002/lpor.202402211

achieving the performance requirements. Consequently, this limits the further development of miniaturized spectrometers.[14]

Over the past decade, an emerging type of miniaturized spectrometer has been designed that leverages a reconstructive algorithm to calculate the incident spectrum from pre-set detection information. The miniaturized reconstructive spectrometer is capable of utilizing a relatively small number of detectors to achieve the objective of detecting spectra with high resolution according to prior knowledge or proper assumptions, which dramatically reduces the footprint of miniaturized spectrometers in principle.[2,15,16] The key point of a reconstructive spectrometer is to construct nonlinear-correlated responsivities for different photodetector channels, which enables the decoding of a high-dimensional spectrum vector.[17–20] A number of material systems have been manufactured successfully with varying optical responsivities including bandgap-engineered nanowires,[21] 2D van der Waals materials,[22,23] in situ dynamically modulated perovskites,[24] colloidal quantum dots,[25] to name a few. The miniaturized reconstructive spectrometers fabricated with those material systems exhibit outstanding performance, whereas the lack of complementary metal oxide semiconductor (CMOS) compatibility or the complex preparation technology limits their large-scale fabrication toward commercialization.

In recent years, driven by the objective of developing low-cost, high-performance, and scalable miniaturized spectrometers, numerous innovative approaches have emerged.[26,27] For instance, Ahamed et al. designed unique hyperspectral responses by integrating periodic surface textures into photodiodes, thereby realizing on-chip miniaturized spectrometers.[28] Concurrently, Zhang et al. developed a miniaturized computational spectrometer based on a plasmonic nanoparticle-in-cavity microfilter array, achieving sub-nanometer spectral resolution.[29] Inspired by the aforementioned advancements, our work focuses on developing a miniaturized spectrometer that aims for a higher degree of integration, utilizes CMOS-compatible wafer-level fabrication processes, features a relatively simpler device architecture, and employs low-cost fabrication techniques. The wedge-shaped structures are constructed on the basis of a silicon-on-insulator (SOI) wafer. The varying thicknesses of Si-NM within its wedge structure exhibit non-linearly correlated optoelectronic properties, rendering it suitable for reconstructive spectrometers. The fabrication process is straightforward and compatible with CMOS large-scale manufacturing technology, making it feasible for wafer-level production of miniature spectrometers. The atomic-level variation in thickness demonstrating by the scanning transmission electron microscopy (STEM) images further enables size reduction of the spectrometer, thereby enhancing device integration capabilities. We have investigated and analyzed the distinctive optical and electrical properties of this structure through both theoretical simulations and experimental studies. Our device with such structure shows the ability to reconstruct spectra in the range from 400 to 1 000 nm. It is also able to resolve peak monochromatic wavelengths with an accuracy of ≈0.1 nm and distinguish between two peak monochromatic wavelengths with a spectral resolution of ≈1.85 nm. We also demonstrate that our Si-NM miniaturized reconstructive spectrometer with wedge-shaped structures has the potential to be applied in the field of hyperspectral imaging. The concept of utilizing wedge-shaped nanomembranes (NMs) as the fundamental basis of miniaturized reconstructive spectrometer also has the potential to be extended to some other types of material systems, such as Germanium-on-insulator structures, for reconstructing spectra in different wavebands or improving the device performance further.

2. Results and Discussion

2.1. The Design and Fabrication of Wedge-Shaped Si-NM Spectrometer

Figure 1a illustrates the principle of the optical response mechanism in a wedge-shaped Si-NM of a SOI wafer. The wedge-shaped Si-NM can be conceptualized as a series of Si-NM channels with various thicknesses, each exhibiting distinct optical properties. According to the Beer-Lambert's law, the intensity I in the z-thickness of the NM can be calculated as:

$$I \propto I_0 e^{-\alpha z} \tag{1}$$

where I_0 is the initial luminous flux and α is absorption coefficient.[30,31] For semiconductor materials, the absorption coefficient is directly related to the wavelength of incident lights λ and the extinction coefficient k, which is

$$\alpha = \frac{4\pi k}{\lambda} \tag{2}$$

Consequently, the penetration depth of light in Si-NM will differ as the change of thickness and wavelength.[32–35] The incident photons are absorbed by the Si-NM within a very short distance for light of short wavelength, while long wavelength light can penetrate totally the thin Si-NM. In addition, the SiO_2 buried oxide (BOX) layer can act as a Fabry-Pérot cavity.[36] When the reflected light waves from the upper and lower Si surfaces meet, the Fabry-Pérot interference will occur.[37,38] As the thickness of Si-NM varies, the optical distance of incident light changes, contributing to the shift of the resonant peaks and the variation of the resonant peak intensities. We calculate the relationship between the absorptance and wavelength of different Si-NM channels, which are displayed in the lower images in Figure 1a and Figure S1 (Supporting Information). From left to right are the absorptance curves corresponding to Si-NM channels with thickness of 50, 200, and 1 000 nm. The absorptance of 50-nm Si-NM channel is relatively low especially in a red and near-infrared waveband. As the thickness of Si-NM channel rises, the absorptance increases and more resonant peaks appear.

The fabrication of the structure of wedge-shaped NMs can be achieved taking advantage of common technologies employed

E. Song, Y. Mei
Shanghai Frontiers Science Research Base of Intelligent Optoelectronics and Perception
Institute of Optoelectronics
Fudan University
Shanghai 200438, P. R. China
Q. Guo
School of Integrated Circuits
Shandong University
Jinan 250100, P. R. China

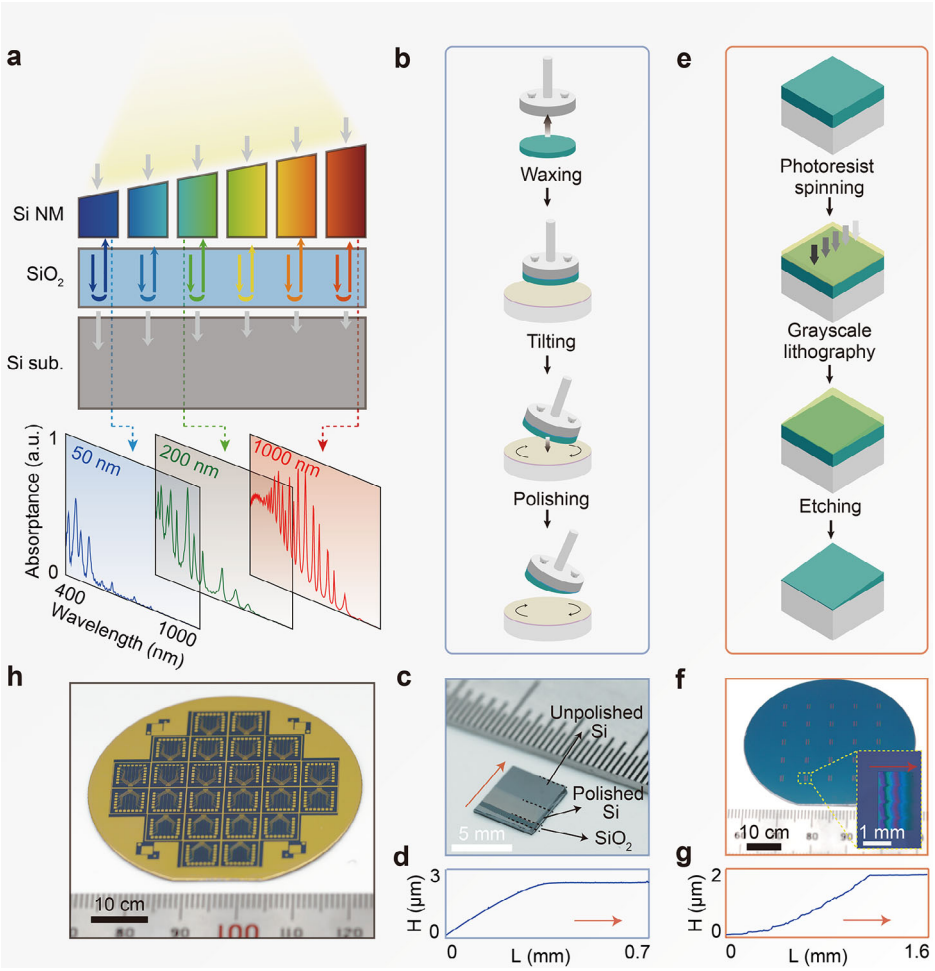

Figure 1. Design and fabrication of wedge-shaped Si-NM spectrometer. a) Schematic diagram of the structure and light absorption of a wedge-shaped Si-NM (top) and the simulated curves between absorptance and wavelength (bottom) with different Si-NM thicknesses. b) Procedure of the CMP fabrication process. c) Photo of a wedge-shaped Si-NM fabricated by CMP process and d) the corresponding related stylus profilometer scan curve along the red arrow. e) Procedures of the grayscale lithography fabrication process. f) Photo of wedge-shaped NM array fabricated by grayscale lithography process. Inset: optical microscopy image of a wedge-shaped NM unit. g) The corresponding stylus profilometer scan curve of a wedge-shaped NM unit along the red arrow. h) The wafer-scale fabrication of the wedge-shaped Si-NM miniaturized spectrometer.

in the CMOS manufacturing process. In our study, two distinct CMOS-compatible preparation methods have been developed for different purposes. Figure 1b depicts a schematic illustration of one fabrication method in which SOI wafers are processed to wedge-shaped NMs by the chemical mechanical polishing (CMP) technique. CMP is a polishing process that can remove the surface materials with a precision control at the molecular scale.[39,40] Usually, the CMP technique is used to flatten the wafer surface by polishing the wafers evenly. However, here we choose to utilize an uneven polishing technique, whereby the polishing direction is tilted. Consequently, only a partial section of the NM will make contact with the polishing plate to be polished. In the experiment, we first glue the sample to the object stage using heated wax and then we can set the object stage to a desired wedging state. Subsequently, the sample is polished by the emery paper and lubricated with polishing solution. The final sample is ground unevenly to produce a wedge-shaped structure. Figure 1c depicts the photograph of a wedge-polished SOI sample. The BOX layer is clearly visible in the naked eye due to the variation in thickness.[41] Furthermore, the polished and unpolished areas of the device layer can be readily distinguished due to the different surface morphologies. Figure 1d presents a characterization of the surface morphology, scanned along the red arrow in Figure 1c. This demonstrates the existence of a wedge-shaped structure with a relatively smooth surface.

Providing that there is a need to realize the large-scale fabrication of wedge-shaped NM array, we can employ the greyscale lithography technique, which is both convenient and cost-effective. This fabrication method has been widely applied in the fabrication 3D structures, such as photonic crystals and phase Fresnel lenses.[42–44] As illustrated in Figure 1e, due to the uniform variation of exposure dose to photoresist, the photoresist layer exhibits a wedge-shape structure after development. Subsequently, an appropriate reactive ion etching (RIE) recipe can be selected to regulate the etch rates in photoresist and NM, thus overcoming the resolution limitation of greyscale lithography.

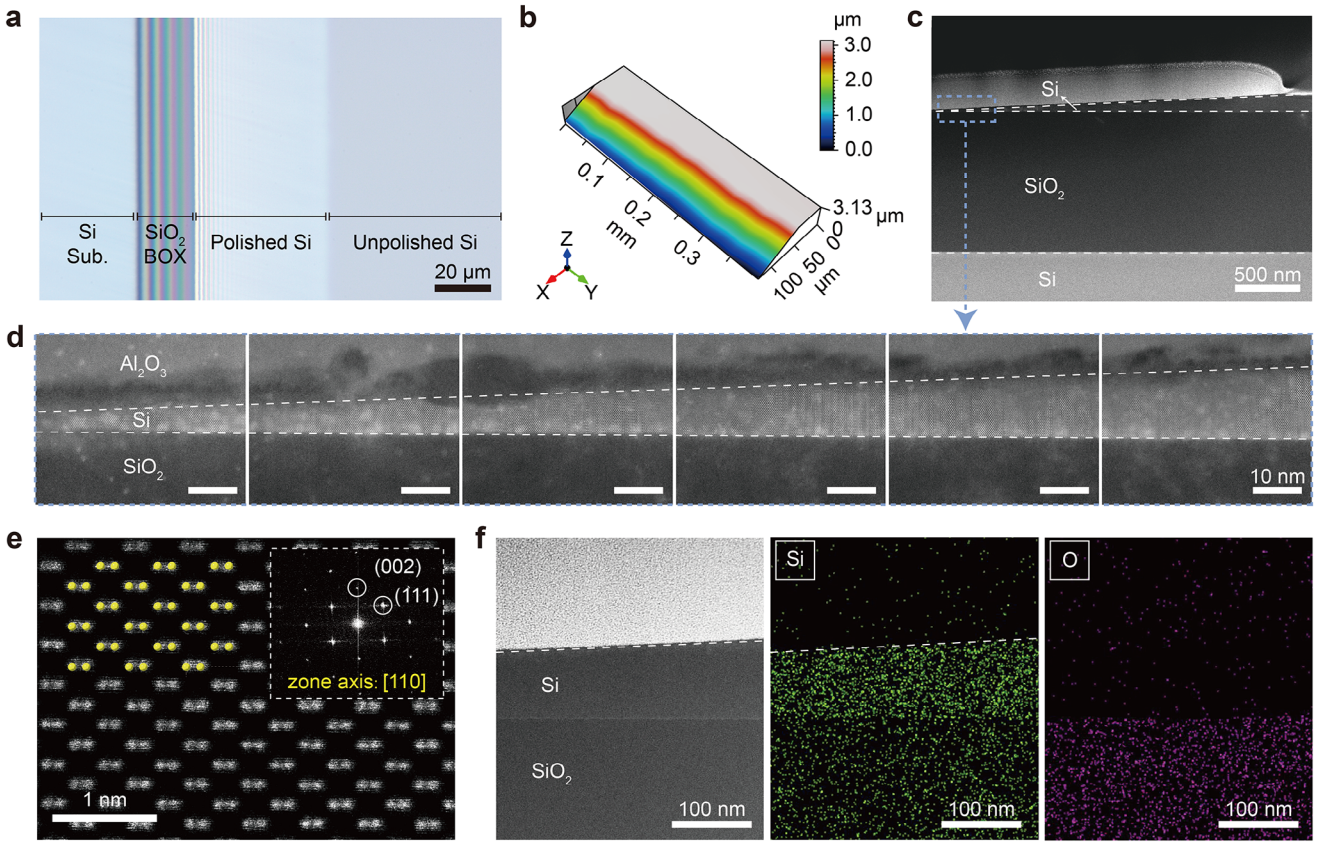

Figure 2. Structural characterization of wedge-shaped Si-NM fabricated by CMP process. a) Optical microscopy image of the surface of the SOI after being wedge polished. Different regions are labeled using line segments. b) 3D topographic scanning of the SOI after being wedge polished. c) Low-magnification cross-sectional STEM image of the SOI with a wedge-shaped Si device layer. The interfaces between different layers in SOI sample are labeled with white dashed lines. d) Zoomed-in high-resolution STEM images. e) Atomic-scale STEM image and standard atomic structure of the Si device layer, viewed along [110] zone axis. Inset: corresponding fast Fourier transform pattern. f) Cross-sectional STEM image of the SOI with a wedge-shaped Si device layer and the corresponding chemical element distribution.

Therefore, the wedge-shaped structure can be transformed into the targeted layer following the RIE process. Figure 1f shows a wedge-shaped NM array fabricated on a 2-inch wafer. The inset is an optical microscopy image of a wedge-shaped NM unit, where the colorful fringes could be distinguished on the sample. Similarly, the stylus profilometer scan reveals the surface profile of the wedge-shaped NM unit (Figure 1g). The scan curve presents several irregular fluctuations, indicating a relatively rough surface. Furthermore, we display a miniaturized reconstructive spectrometer array fabricated in a wafer-scale based on the wedge-shaped NM structure array in Figure 1h, showing that it is possible to fabricate miniaturized spectrometer arrays in a wafer scale. We performed a characterization analysis of the array structure's uniformity (Figure S2, Supporting Information). The experimental data verified the high manufacturing precision and excellent uniformity of the wedge-shaped array structure.

2.2. Structural Characterization of Wedge-Shaped Si-NM Spectrometer

Figure 2a gives an optical microscopy image of the wedge-shaped Si-NM in SOI wafer fabricated by the wedge polishing process. We can clearly observe the colorful fringes of SiO_2 BOX layer as its thickness is gradually varied. The distinct colors of SiO_2 are indicative of specific thicknesses, which allows for the estimation of the slope of the wedge-shaped Si-NM. For further precise measurement on the surface topography of wedge-shaped Si device layer, a 3D topographic scanning is shown in Figure 2b. From the mapping data we can find that the wedge structure has a 62.88-μm length and a 3.13-μm length. Hence the slope is calculated to be 1:20, which is close to the slope of our design. We also demonstrate the fabrication of wedge-shaped Si-NMs with other slopes in Figure S3 (Supporting Information). The same structural characterization is also carried out on the sample fabricated by greyscale lithography technique (Figure S4, Supporting Information), demonstrating the existence of the wedge-shaped structure in such sample.

In order to observe the cross-section, a sample at the wedge-polished Si device layer was cut by focused ion beam (FIB) etching. The side view of the SOI with a wedge-shaped Si device layer is shown in Figure 2c. The interfaces between different layers in SOI sample are labeled with white dashed lines. We can find a very regular increase of the thickness in the Si device layer at the microscopic scale. A set of high-resolution STEM images of the thinnest part of wedge-shaped Si device layer is displayed in

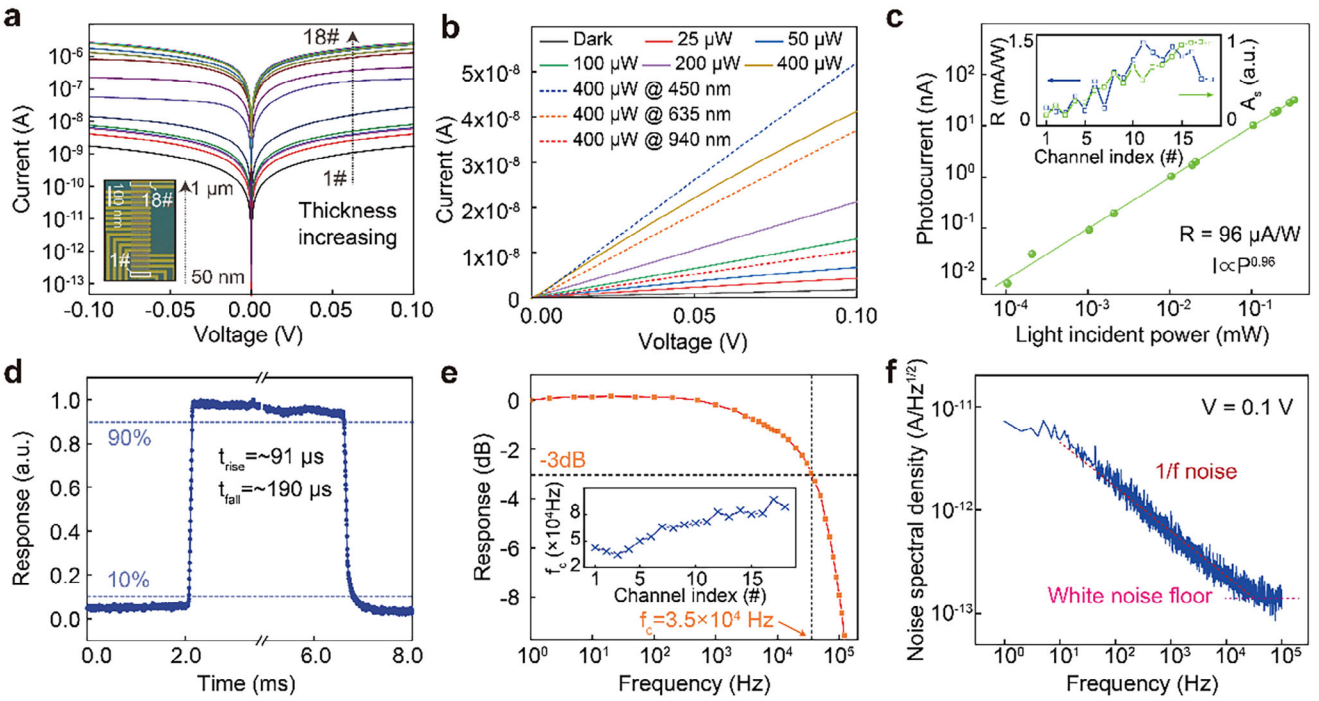

Figure 3. Performance of wedge-shaped Si-NM photodetector fabricated by CMP process. a) I-V curves in dark measured at each photodetector channel. Inset: optical microscopy image of Si photodetector arrays on the wedge-shaped spectrometer. b) Measured I-V curves of the Si photodetector channel with the thinnest thickness, illuminated by a 520-nm laser with different powers (solid lines) and lasers with different wavelengths (dashed lines). c) LDR property of the same Si photodetector channel at 0.1 V bias. Inset: the responsivity R and simulated value A_s of 18 channels. d) Response time of the same Si photodetector channel at 0.1 V bias. The rise and fall time are measured as ≈91 and ≈190 μs, respectively. e) Frequency response of the same Si photodetector channel at 0.1 V bias. The cut-off frequency f_c is measured as 3.5×10^4 Hz. Inset: the measured cut-off frequency f_c of 18 channels. f) Current noise of the same Si photodetector channel as a function of frequency.

Figure 2d, from which the increasing thickness of Si-NM in an atomic scale can be clearly observed. The atomic image is captured in the Si-NM as thin as ≈2 nm, indicating that the quality of Si-NM is not significantly impacted after polishing process. Some pits and defects can be observed on the upper surface of Si-NM, which might be caused by the scratches during the process of polishing or the impurity particles.[45,46] Figure 2e shows a lattice-resolved STEM image of Si viewed along [110] zone axis from the wedge-shaped Si device layer. The two adjacent Si atoms can be clearly resolved with a 0.135-nm dumbbell spacing along vertical Si [001] orientation. The captured atomic structure is highly consistent with diamond structure of single-crystalline Si, demonstrating that the Si device layer maintains an excellent single-crystalline structure after processing.[47] The corresponding fast Fourier transform pattern is represented in the inset, while the selected area electron diffraction pattern is shown in Figure S5 (Supporting Information). The presence of distinct diffraction points signifies the preservation of the single-crystalline structure in the Si device layer. The characteristic element maps of the cross section are obtained by energy-dispersive X-ray spectroscopy (EDS), displayed in Figure 2g. The atomic-level resolution STEM image, together with the corresponding chemical element distribution, is presented in Figure S6 (Supporting Information). Si and O contents are clearly identified and marked with green color and purple color, respectively. Here, the upper surface of Si-NM is indicated by the white dashed line, and thus the element distribution mapping also corroborates the presence of a wedge-shaped structure. Furthermore, the distribution of elements exhibits a clearly differentiated interface demonstrating that the SOI sample maintains its surface morphology quality after processing.

2.3. Electrical Properties and Optoelectrical Characteristics of Wedge-Shaped Si-NM Photodetector

A wedge-shaped Si photodetector array, featuring varying thicknesses, is fabricated using a wedge-shaped Si-NM structure from a SOI wafer (Figure S7, Supporting Information). The Si-NM structure, which has a slope of ≈1:500, is chosen for this purpose. It is segmented into 18 photodetector channels, each characterized by a uniformly varying thickness. The thinnest photodetector channel is designed as 50 nm, while the thickest is 1 000 nm. The electrical properties of each photodetector channel within the array are assessed, as depicted in **Figure 3a**. It can be observed that the dark currents exhibit an increase trend with the increasing thickness. The observed variation in dark currents can be attributed to the variation of resistance as well as the difference on the impact of surface or interface states.[46,48,49] The inset in Figure 3a shows the optical microscopy image of the wedge-shaped Si-NM with an array of parallel Cr/Au electrodes. The arrows indicate the direction in which the NM thickness increases. The footprint of a single photodetector channel is designed as 10×100 μm^2. Figure 3b exhibits the typ-

ical I-V curves of the thinnest wedge-shaped Si-NM photodetector channel under illumination with lasers of various wavelengths and power levels. The stable and linear optoelectrical response demonstrates that the thinnest channel exhibits promising optoelectrical properties. The symmetrical current-voltage (I-V) curves indicate that these detectors exhibit characteristics typical of Metal-Semiconductor-Metal photodetectors. More detailed I-V analysis and scanning photocurrent mapping results are presented in the Figure S8 (Supporting Information). The optical response characteristics at various operating voltages are presented in the Figure S9 (Supporting Information). Based on these comprehensive experimental results, an operating voltage of 0.1 V was selected. Figure 3c depicts the linear dynamic response (LDR) of the same photodetector channel under illumination of a 520-nm laser source with power ranging from ≈10 nW to 0.33 mW, which is calculated to be ≈70 dB. The LDR properties of this photodetector channel illuminated by the laser sources with other wavelengths are also shown in Figure S10 (Supporting Information), indicating a good linear optical responsivity in the visible and near-infrared wavelength band. It is worth noticing that a robust linear response is crucial for the analysis-based spectral reconstruction algorithms, as the intensity of incident light is unknown when reconstructing the spectra. It is essential to guarantee that the optical response matrix does not change nonlinearly when performing different spectral reconstruction with underlying linear algebra assumptions. According to the relation between photocurrent and incident light power, the responsivity is calculated to be 96 μA W^{-1}. The LDR characteristics of each photodetector channel are also measured (Figure S11, Supporting Information), and the corresponding responsivities R with the simulated absorptances A_s are shown in the inset of Figure 3c. The channel numbers, from smallest to largest, correspond to the thinnest photodetector channel to the thickest. A general upward trend in both R and A_s can be found as the thickness increases. A periodic change also exists on account of the interference phenomenon. The slight difference between R and A_s might be owing to a discrepancy between the designed thicknesses and the actual values, as well as the influence of other optoelectrical mechanisms, such as the optical response of the Schottky junction between the electrode metal and Si or the response due to impurity or defect-related absorption.[50,51]

Figure 3d shows the responsive time of the photodetector under a chopped pulse square wave laser illumination. The rise time (the response increasing from 10% to 90% of the maximum value) and fall time (from 90% to 10%) are measured as ≈91 and ≈190 μs, respectively, indicating the rapid response of the photodetector. The responsive times of all channels are displays in Figure S12 (Supporting Information). To determine the response bandwidth of the photodetector, we measure the frequency response and consider the frequency at which the response drops to −3 dB of the value in low frequency as the cut-off frequency (f_C),[52] and the obtained f_C of 3.5×10^4 Hz is shown in Figure 3e. The response speed and frequency response of other channels are also measured (see inset of Figure 3e). In general, the response speed and frequency response performance across all channels are comparable in magnitude, while the cut-off frequencies are slightly lower for the relatively thinner channels due to their increased susceptibility to trapping states.[53] Figure 3f shows the noise spectral density at the bias of 0.1 V. The analysis indicates that 1/f noise is the primary source of noise for this device at relative low frequencies, whereas white noises such as shot noise and thermal noise become more noticeable at higher frequencies above $\approx 3 \times 10^4$ Hz. The results of the photoelectric response stability test, provided in the Figure S13 (Supporting Information), showcase the robust stability of the Si-NM photodetector amidst fluctuating room temperature conditions. The performance of wedge-shaped Si-NM photodetector fabricated by greyscale lithography technique is shown in Figure S14 (Supporting Information), which is comparable with that fabricated by CMP process.

2.4. Spectrum Reconstruction Characterization of Wedge-Shaped Si-NM Spectrometer

In order to computationally reconstruct the unknown spectrum, the initial step is to calibrate the light responsivity of the spectrometer. This is achieved by mapping the photocurrent when irradiated by monochromatic lights with different wavelengths. A Xenon lamp with a monochromator is used to split the lights ranging from 400 to 1 000 nm, and 300 photocurrent values are obtained with a 2-nm step for every photodetector channel. The responsivity of the spectrometer as a function of the channel number and wavelength has been calculated and the result is exhibited in **Figures** 4a and S15 (Supporting Information). The wedge structure with designed thickness of each channel is also displayed. A regular movement of photoresponsivity peaks can be found with the rising of thickness of photodetector channel. Figure 4b depicts the computationally spectrum reconstruction workflow. The pre-calibrated response matrix $R(\lambda)$ displayed in Figure 4a, along with the measured photocurrent I can be used to reconstruct the unknown spectrum $S(\lambda)$ by solving a system of linear equations:

$$\int_{\lambda_1}^{\lambda_2} S(\lambda) \cdot R_i(\lambda)\, d\lambda = I_i \tag{3}$$

where λ_1 and λ_2 are the start and end wavelength of the response range, respectively. In contrast to traditional spectrometers, the spectral resolution of our spectrometer is not directly proportional to the number of detected channels. For a spectrometer with n photodetector channels, there are n equations in the system. To solve the aforementioned equations, the continuous signal $S(\lambda)$ needs to be reconstructed to a discrete vector through a linear combination of m kernel functions. The Gaussian function is selected as the kernel function here due to its shape being similar to the contour shape of the spectral lines emitted by the light source.[54] Accordingly, the number of Gaussian functions employed (i.e., m) directly determines the resolution of the reconstructed spectra. Due to the limited footprint of the miniaturized spectrometer, it might be impossible to select an excessive number of photodetector channels n.[2,5] In order to achieve high accuracy in the reconstruction of the spectra, the number of Gaussian functions m to be fitted should be considerably larger than that of photodetector channels n. This results in an underdetermined system of equations, which cannot be solved using traditional iterative methods.[25,55] To address this issue, our code incorporates Tikhonov regularization to minimize the residual

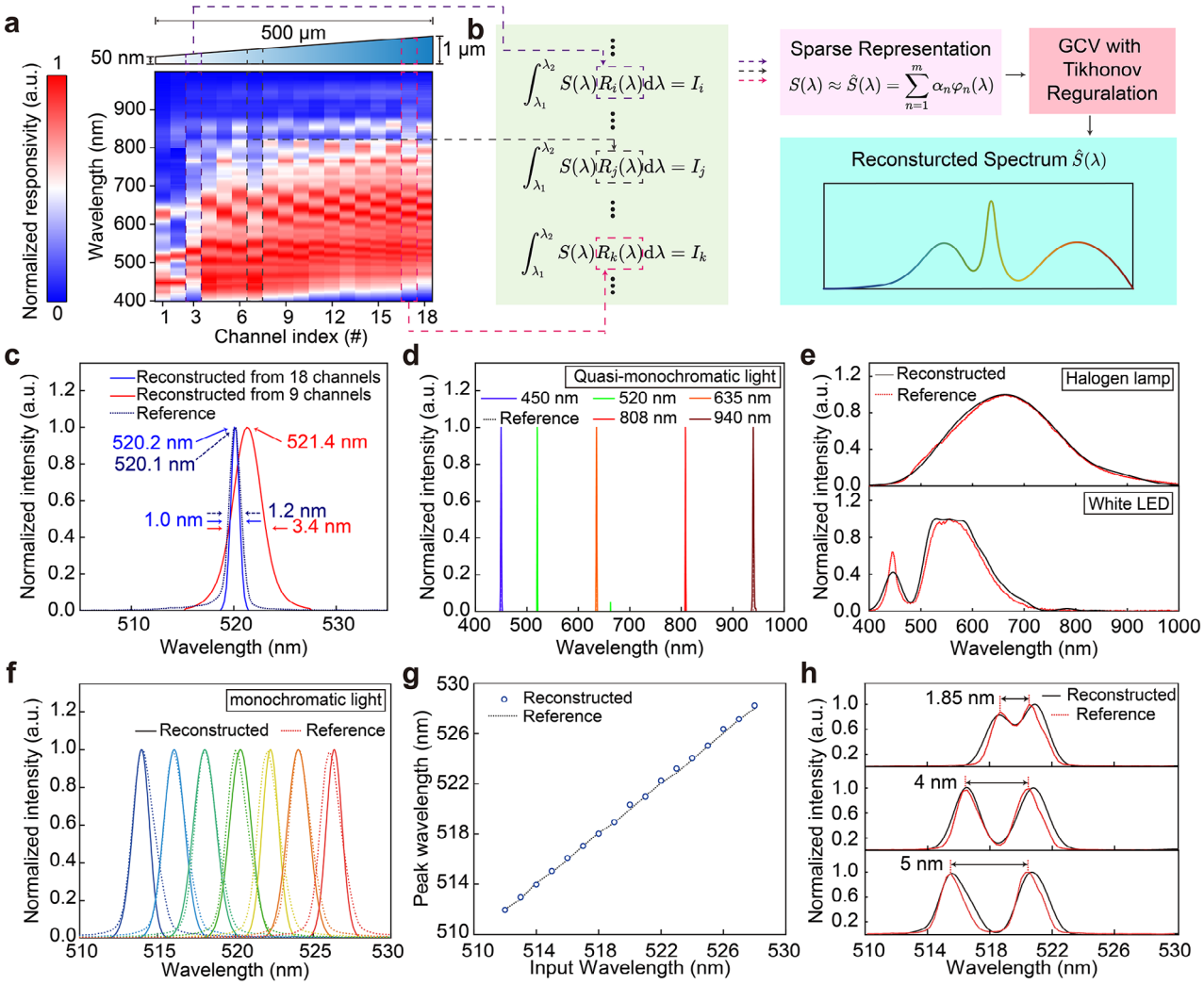

Figure 4. Spectrum reconstruction of wedge-shaped Si-NM spectrometer fabricated by CMP process. a) Normalized response matrix mapping of our spectrometer. The structure of the wedge and designed thickness of each photodetector channel is plotted on the top. b) Schematic illustration of the process of spectrum reconstruction. c) A spectral peak at 520 nm reconstructed from 18 channels (blue solid curves) and 9 channels (red solid curves). Reference spectrum measured by a commercial spectrometer (dashed curves) is also shown for comparison. d) The reconstructed spectra under the illumination of quasi-monochromatic lights with different wavelengths (solid curves) and the reference spectra measured by a commercial spectrometer (dashed curves). e) The reconstructed spectra under the illumination of two different wide-band light sources (solid curves) and the reference spectra measured by a commercial spectrometer (dashed curves). f) Monochromatic spectra reconstructed with our spectrometer (solid curves) and measured by a commercial spectrometer (dashed curves). g) Comparison of the peak wavelengths determined from the reconstructed spectra and the reference spectra by a conventional spectrometer. h) Spectra of the mixture of two monochromatic light sources reconstructed with our spectrometer (solid curves) and measured by a commercial spectrometer (dashed curves).

norm, along with the generalized cross-validation (GCV) method to determine the appropriate regularization parameter.[21–23] This reconstructive algorithm requires the sparsity of the measured spectrum, and consequently, it is necessary to select appropriate parameters for the Gaussian functions in order to transform the measured spectrum data into a signal vector as sparsely as possible.[56]

In order to demonstrate the ability of our wedge-shaped Si-NM spectrometer to reconstruct different types of spectra, we conducted a series of measurements in the wavelength range of 400–1 000 nm with our spectrometer. In order to ascertain the impact of the number of channels on the accuracy of the reconstructed spectra, we selected two different spectrometers, containing 9 and 18 photodetector channels respectively, to reconstruct a monochromatic light source. The measurement and reconstruction of a spectral peak at 520 nm was performed by using all the 18 channels and 9 channels (Figure 4c). Compared to the spectrum reconstructed by 9 channels, the spectrum reconstructed by 18 channels demonstrates a closer full-width at half-maximum (FWHM) and peak values to the spectrum measured by a commercial spectrometer. This indicates that the spectrometer with 18 channels has sufficient capacity for precise spectral reconstruction, given the trade-offs between performance and footprint. Several reconstructed quasi-monochromatic spectra obtained by our spectrometer with 18 channels are also in good agreement with the reference spec-

tra (Figure 4d; Figure S16, Supporting Information), thereby demonstrating that our spectrometer can distinguish the quasi-monochromatic lights with high accuracy in the waveband ranging from visible to near-infrared range. Moreover, our spectrometer's reconstruction capabilities remain consistently outstanding when faced with broadband spectra. Figure 4e shows that the broadband spectra illuminated by a halogen lamp and a white light-emitting diode (LED) can also be reconstructed by our spectrometer. A slight discrepancy exists between the spectra obtained by reconstructive spectrometer and the ground truth spectra measured by the commercial spectrometer. This is due to the fact that some relatively complex spectra, such as the spectrum emitted by LEDs, lack desired sparsity for a common-used discretized representation by using the Gaussian functions as kernel function to fit the spectrum. Increasing the number of channels or improving the performance of photodetectors to reduce the impact of noises can be effective means of enhancing the resolving power of our spectrometer in further work.[21] Similarly, Figure S17 (Supporting Information) displays the optical response matrix and spectral reconstruction results of the wedge-shaped spectrometer fabricated using the greyscale lithography process, demonstrating its capability for spectral reconstruction as well. Due to the Fabry-Pérot cavity's sensitivity to the incident light angle (Figure S18, Supporting Information), the aforementioned spectral reconstruction experiments utilized an optical collimator to ensure normal incidence of the light beam. In practical applications, scenarios involving obliquely incident light may be encountered. To evaluate the tolerance for deviations in the incident angle and to identify effective solutions, we conducted a series of experiments, which are detailed in the Figures S19 and S20 (Supporting Information).

To characterize the wavelength-resolving power of our spectrometer, a high-resolution spectral response matrix with a 0.1-nm resolution in a 20 nm wavelength band from 510 to 530 nm is pre-measured (Figure S21, Supporting Information). The pairwise correlation coefficient among the response function vectors is calculated (Figure S22, Supporting Information). We measure the response currents from several monochromatic lights with FWHM of ≈2 nm and reconstruct corresponding spectra, with a portion of these results displayed in Figure 4f (related experimental setup is shown in Figure S23, Supporting Information). The deviation compilation between the input peak wavelengths and the output reconstructed peak wavelengths is depicted in Figure 4g. The average peak wavelength deviation is calculated to be ≈0.1 nm (Figure S24a, Supporting Information) and the average wavelength-resolving power ($R_\lambda = \lambda/\Delta\lambda$) reaches up to ≈$10^4$ (Figure S24b, Supporting Information). As is revealed in Figure 4h, we generate a series of spectra by using two monochromatic lights with diverse peak spacings to estimate the spectral resolution (related experimental setup is shown in Figure S25, Supporting Information). Our spectrometer can clearly resolve the two single peaks in the spectrum with a minimum wavelength spacing of 1.85 nm, showcasing its exceptional resolution down to the nanometer scale. Moreover, the simulation evaluates the influence of random noise on the reconstruction performance. It is evident from Figure S26 (Supporting Information) that the spectrometer is capable of effectively mitigating the effects of noise. We calculated various metrics, including the Root Mean Square Error, Peak Signal-to-Noise Ratio, Coefficient of Determination and the fidelity, to quantitatively evaluate the spectral reconstruction performance. The results are summarized in Table S1 (Supporting Information). These quantitative characterization outcomes demonstrate the robust spectral reconstruction capabilities of the miniature spectrometer. Comparison of characteristics and performances of other miniaturized reconstructive spectrometers is shown in Table S2 (Supporting Information).

2.5. Applications in Hyperspectral Imaging by Wedge-Shaped Si-NM Spectrometer

With high compatibility with CMOS process, micrometer-scale footprint, and extraordinary spectrum reconstruction performance, our spectrometer has potential to be considered as a suitable foundation for future compact on-chip integrated spectral imaging components. Hyperspectral images typically comprise hundreds of consecutive spectral channels and are rich in spatial and spectral information, which is an important technique widely applied in the field of agriculture,[57,58] clinical medicine,[59,60] etc. Here we design a spatial scanning system based on our spectrometer to demonstrate the application of hyperspectral imaging (**Figure 5a**). We used a white light LED source as the backlight and various colored filters to create the desired "Si" pattern, specifically designed for evaluating hyperspectral imaging performance. The transmitted light is focused by lens onto the spectrometer and then the image plane is scanned across the focal plane. The response current data at each "pixel" is measured along the scanning process, thus enabling the reconstruction of the spectral data cube, from which the hyperspectral images reconstructed at different wavelengths can be obtained (Figure 5b). In comparison to traditional red-green-blue images, hyperspectral images offer a significant enhancement in the quantity and quality of the conveyed information. To illustrate the results more intuitively, the spectral power distributions were converted into International Commission on Illumination 1931 chromaticity coordinates, allowing for the creation of visual representations. Figure 5c displays the reconstructed pseudo-colored spectral image of the "Si" pattern, performing consistency with the original image (Figure 5d). Furthermore, the reconstructed spectra of four colors are in good agreement with conventional spectrometer measurements of the corresponding points, as is shown in Figure 5e. The spectrometer's capability to concurrently analyze spectral characteristics (related to wavelengths) and spatial data (related to physical locations or positions) enables comprehensive data integration and interpretation.

3. Conclusion

In summary, we have developed a miniaturized Si-NM reconstructive spectrometer utilizing an array of Si photodetectors with varying NM thicknesses, achieved through wedge-shaped structures via a CMOS-compatible fabrication process. The modulation of the optical response due to variations in the thickness of the Si-NM photodetector simplifies the spectrometer structure and substantially reduces device preparation cost. The integration of such miniaturized spectrometers is significantly enhanced by leveraging atomic-level control over NM thickness in

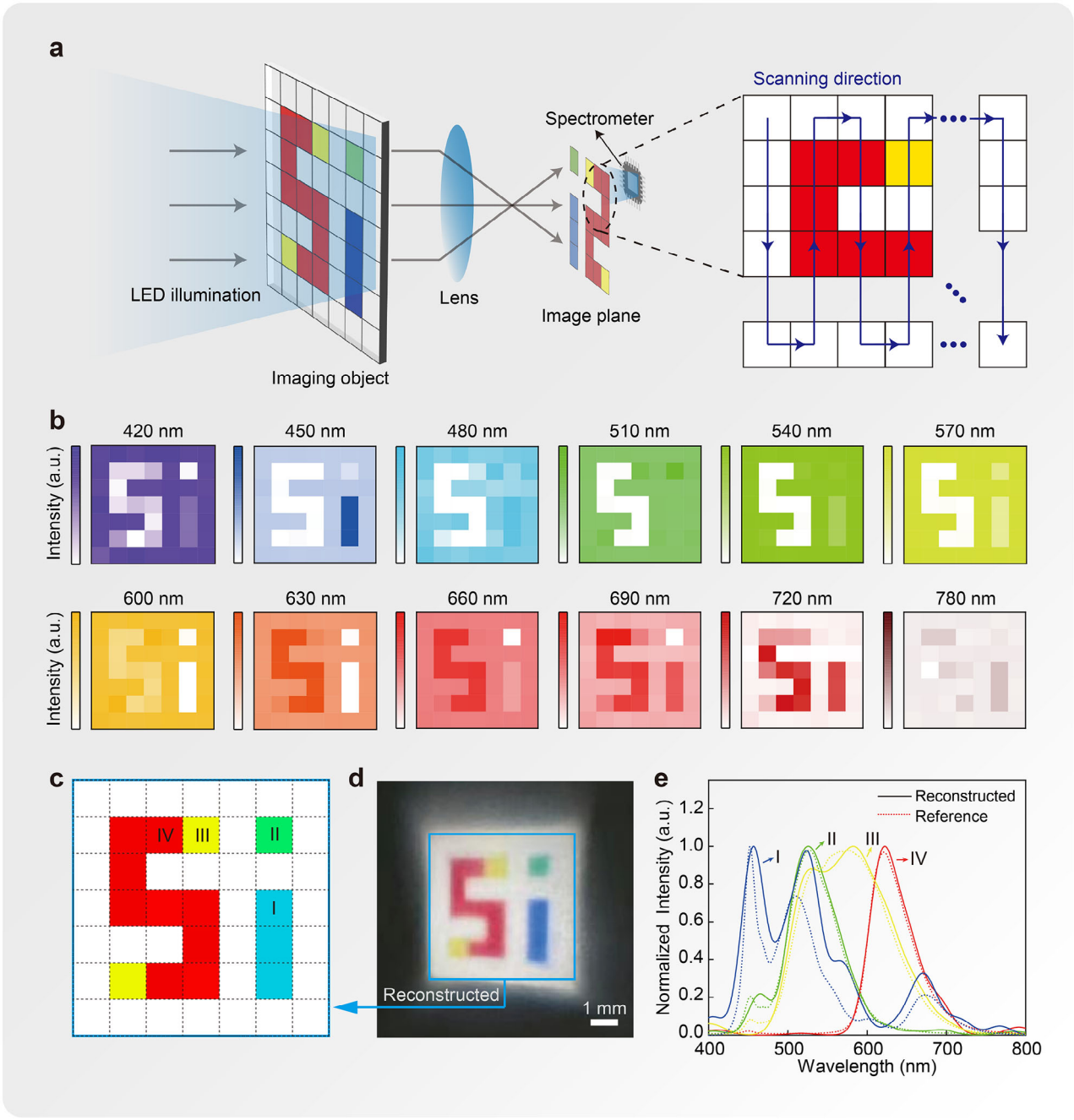

Figure 5. Hyperspectral imaging by wedge-shaped Si-NM spectrometer. a) Schematic of the hyperspectral imaging system prepared based on our spectrometer. The scanning speed is ≈0.28 mm s^{-1}. b) Reconstructed hyperspectral images at different wavelengths. The pixel intensity is normalized within each pixel. c) Reconstructed pseudo-colored spectral image. d) Image pattern photographed by a CMOS camera. e) Reconstructed spectra of four different colors (solid curves) and corresponding measured spectra by a commercial spectrometer (dashed curves).

wedge-shaped architectures. We present an array of 18 channels configured as a miniaturized spectrometer, covering the entire visible and near-infrared spectrum ranging from 400 nm to 1 000 nm. Our spectrometer achieves high-resolution spectral reconstruction with an ≈1.85-nm resolution and an average 0.1-nm spectral wavelength accuracy, within a compact active area at the micrometer scale. Furthermore, our proof-of-concept demonstrates its capability for hyperspectral imaging, highlighting its versatility and potential across diverse applications. This research paves the way for developing miniaturized spectroscopy systems that not only maintain superior performance, but also seamlessly integrate with contemporary CMOS technologies, promising substantial advancement in spectral analysis and imaging applications.

4. Experimental Section

Finite-Difference Time Domain (FDTD) Simulations: FDTD simulations were used to determine the absorptance of the Si-NM in the SOI structure. The absorptance spectra were obtained using the planewave source and perfectly matched layer boundary condition in the direction parallel to the substrate to minimize any potential distortion of the results, while the periodical boundary condition was applied in the direction perpendicular to the substrate. The thickness of insulator layer was set as 1 000 nm. Two frequency-domain fields and power monitors were set at the top and down of silicon NM to calculate the absorptance.

Fabrication of the Wedge-Shaped Si-NM: CMP Process: A polishing machine (Allied MultiPrep System, 8″) was used to demonstrate the fabrication of a wedge-shaped Si-NM by CMP process. The SOI sample was first cleaned and then adhered to the fixture by wax. The polishing side should be faced down and attached to the diamond lapping film on the platen. The sample was tilted controlled by the micrometers on the polishers so that an angle was introduced to the sample and the wedge-shaped structure was created.

Fabrication of the Wedge-Shaped Si-NM: Greyscale Lithography Process: The photoresist S1813 was spin-coated on the SOI sample and prebaked at 90 °C for 90 s. Then the sample was exposed with grayscale UV laser dose by UV laser direct-writing system (Durham Magneto Optics, ML3 aligner). The linearly graduated greyscale pattern was chosen to produce a continuous and uniform variation in the UV lithography intensity so that the photoresist assumes a wedge-shaped structure after development. The following RIE process (Samco RIE-10NR) can etch the Si layer to form wedge-shaped structure the same as the photoresist layer. RIE was performed at pressure of 6 Pa, 35 sccm CHF_3 + 2 sccm SF_6, RF power of 100 W.

Fabrication of the Device: The photolithography technique was employed to define the Si-NM patterns to form channels with different thicknesses. The Si-NM parts which were not covered by the photoresist were etched by RIE process (Trion T2). RIE was performed at pressure of 100 mTorr, 3 sccm O_2 + 15 sccm SF_6, RF power of 50 W. The Cr/Au layers were deposited by using magnetron sputtering system (DE Technology, DE500). The thicknesses of Cr and Au layers are 10 and 200 nm, respectively. Then the metal layer was patterned by the photolithography technique and wet etched to form the electrodes. The electrodes were arranged in parallel along the direction of thickness variation to capture the photocurrent generated from each segment of the wedge-shaped structure.

Structural Characterization: The 3D topographic scanning of wedge-shaped Si-NM was characterized by stylus profiler (KLA-Tencor Corp, AlphaStep D-600). The cross-section lamella was cut by FIB with the protection of the deposited SiO_2 and Pt layers. The insulator protective layer deposited by atomic layer deposition can avoid the top device layer being damaged by ion bombardment during the FIB sampling process. The STEM images and EDS measurements were performed by JEOL JEM-ARM200F TEM.

Optoelectronic Performance Tests: The electrical properties of the spectrometer were obtained by using a precise source meter (Keysight B2902B). The value of photocurrent was evaluated under modulated laser irradiation (Lei Ze Electronics), and the signal was acquired by a lock-in amplifier (Sine Scientific Instrument OE1022D) with a current amplifier (Stanford SR570). The responsivity time of the device was measured by using an oscilloscope (Tektronix TBS2000) under a pulsed laser irradiation modulated by a signal generator (Keysight 33500B). The current noise was measured by a semiconductor parameter analyzer (Primarius FS-Pro). Light power of different sources was measured by an optical power meter (Thorlabs PM100D). A Xenon lamp with a monochromator (Zolix TLS300X) was used to output the monochromatic lights with different wavelengths so that the response matrix of the spectrometer could be calibrated.

Reconstruction Process: The reconstruction process can be divided into three parts, which are learning process, measuring process, and calculating process. In the learning process, a spectral response matrix $\boldsymbol{R}$ of the spectrometer is needed to be calibrated which contains responsivity from different response channels at different wavelengths. In the measuring process, the photocurrents of each response channel are measured when illuminated by the light source with unknown spectrum $S(\lambda)$, where the photocurrent vector $\boldsymbol{I}$ can be obtained. A linear combination of n Gaussian basis functions $\varphi_n(\lambda)$ are utilized to sparsely discretize the continuous $S(\lambda)$. The peaks of the Gaussian functions are generated as a linearly spaced vector in the wavelength range. Therefore, the spectrum curve can be represented as a vector $\boldsymbol{S}$, which can be calculated by the formula: $\boldsymbol{S} \times \boldsymbol{R} = \boldsymbol{I}$. In the calculating process, this formula is needed to be solved to calculate the spectrum vector $\boldsymbol{S}$. To find the best solution, we need to find a spectrum vector $\boldsymbol{S}$ to minimize the residual norm, $\|\boldsymbol{S} \times \boldsymbol{R} - \boldsymbol{I}\|^2$. To enhance solution stability and noise robustness, a regularization factor γ, also referred to as Tikhonov regularization, is introduced. This factor modifies the objective by minimizing the cost function, $\|\boldsymbol{S} \times \boldsymbol{R} - \boldsymbol{I}\|^2 + \gamma^2 \|\boldsymbol{S}\|^2$. Here, the GCV method was introduced to select the suitable regularization factor γ, and the calculation process was implemented by using a Python script.

Supporting Information

Supporting Information is available from the Wiley Online Library or from the author.

Acknowledgements

This work is supported by the National Key Technologies R&D Program of China (No. 2021YFA0715302), the National Natural Science Foundation of China (Nos. 62375054 and 523B2107), and the Science and Technology Commission of Shanghai Municipality (No. 24520750200). Part of the experimental work was carried out in Fudan Nanofabrication Laboratory.

Conflict of Interest

The authors declare no conflict of interest.

Author Contributions

Y.H. and C.Y. contributed equally to this work. Y. Mei, Y. Hu, and C. You conceived the idea for the project and designed the experiments. Y. Hu, C. You, B. Wu, Z. Zhang, C. Liu, J. He, and B. Chen fabricated the devices and performed the electronic and optoelectronic measurements. Y. Hu, C. You, Z. Zheng, Z. Qiao, M. Ma, and T. Cai performed structural characterization. Y. Hu, C. You, G. Huang, and Y. Mei co-wrote the manuscript. All authors discussed the results and commented on the manuscript.

Data Availability Statement

The data that support the findings of this study are available from the corresponding author upon reasonable request.

Keywords

CMOS-compatible integration, hyperspectral imaging, single-crystalline Si nanomembranes, spectrometers, spectrum reconstruction

Received: December 18, 2024
Revised: June 5, 2025
Published online: June 25, 2025

[1] L. P. Schuler, J. S. Milne, J. M. Dell, L. Faraone, *J. Phys. D: Appl. Phys.* **2009**, *42*, 133001.
[2] Z. Yang, T. Albrow-Owen, W. Cai, T. Hasan, *Science* **2021**, *371*, abe0722.

[3] R. F. Wolffenbuttel, *IEEE Trans. Instrum. Meas.* **2004**, *53*, 197.
[4] M. Ebermann, N. Neumann, K. Hiller, M. Seifert, M. Meinig, S. Kurth, *Proc. SPIE* **2016**, *9760*, 97600H.
[5] A. Li, C. Yao, J. Xia, H. Wang, Q. Cheng, R. Penty, Y. Fainman, S. Pan, *Light: Sci. Appl.* **2022**, *11*, 174.
[6] N. Savage, *Nat. Photonics* **2009**, *3*, 601.
[7] R. A. Crocombe, *Appl. Spectrosc.* **2018**, *72*, 1701.
[8] N. Blind, E. Le Coarer, P. Kern, S. Gousset, *Opt. Express* **2017**, *25*, 27341.
[9] M. Faraji-Dana, E. Arbabi, A. Arbabi, S. M. Kamali, H. Kwon, A. Faraon, *Nat. Commun.* **2018**, *9*, 4196.
[10] A. Tittl, A. Leitis, M. Liu, F. Yesilkoy, D.-Y. Choi, D. N. Neshev, Y. S. Kivshar, H. Altug, *Science* **2018**, *360*, 1105.
[11] S.-W. Wang, C. Xia, X. Chen, W. Lu, M. Li, H. Wang, W. Zheng, T. Zhang, *Opt. Lett.* **2007**, *32*, 632.
[12] D. Pohl, M. Reig Escalé, M. Madi, F. Kaufmann, P. Brotzer, A. Sergeyev, B. Guldimann, P. Giaccari, E. Alberti, U. Meier, R. Grange, *Nat. Photonics* **2019**, *14*, 24.
[13] S. N. Zheng, J. Zou, H. Cai, J. F. Song, L. K. Chin, P. Y. Liu, Z. P. Lin, D. L. Kwong, A. Q. Liu, *Nat. Commun.* **2019**, *10*, 2349.
[14] U. Kurokawa, B. I. Choi, C. C. Chang, *IEEE Sens. J.* **2011**, *11*, 1556.
[15] W. Deng, C. You, Y. Zhang, *IEEE Sens. J.* **2021**, *21*, 4044.
[16] S. Yuan, C. Ma, E. Fetaya, T. Mueller, D. Naveh, F. Zhang, F. Xia, *Science* **2023**, *379*, ade1220.
[17] W. Hartmann, P. Varytis, H. Gehring, N. Walter, F. Beutel, K. Busch, W. Pernice, *Adv. Opt. Mater.* **2020**, *8*, 1901602.
[18] Z. Xuan, Z. Wang, Q. Liu, S. Huang, B. Yang, L. Yang, Z. Yin, M. Xie, C. Li, J. Yu, S. Wang, W. Lu, *Adv. Opt. Mater.* **2022**, *10*, 2200284.
[19] B. Redding, S. F. Liew, R. Sarma, H. Cao, *Nat. Photonics* **2013**, *7*, 746.
[20] C. You, X. Li, Y. Hu, N. Huang, Y. Wang, B. Wu, G. Jiang, J. Huang, Z. Zhang, B. Chen, Y. Wu, J. Liu, X. Chen, E. Song, J. Cui, P. Zhou, Z. Di, Z. An, G. Huang, Y. Mei, *Proc. Natl. Acad. Sci. U. S. A.* **2024**, *121*, 2403950121.
[21] Z. Yang, T. Albrow-Owen, H. Cui, J. Alexander-Webber, F. Gu, X. Wang, T.-C. Wu, M. Zhuge, C. Williams, P. Wang, A. V. Zayats, W. Cai, L. Dai, S. Hofmann, M. Overend, L. Tong, Q. Yang, Z. Sun, T. Hasan, *Science* **2019**, *365*, 1017.
[22] M. G. Uddin, S. Das, A. M. Shafi, L. Wang, X. Cui, F. Nigmatulin, F. Ahmed, A. C. Liapis, W. Cai, Z. Yang, H. Lipsanen, T. Hasan, H. H. Yoon, Z. Sun, *Nat. Commun.* **2024**, *15*, 571.
[23] H. H. Yoon, H. A. Fernandez, F. Nigmatulin, W. Cai, Z. Yang, H. Cui, F. Ahmed, X. Cui, M. G. Uddin, E. D. Minot, H. Lipsanen, K. Kim, P. Hakonen, T. Hasan, Z. Sun, *Science* **2022**, *378*, 296.
[24] L. Guo, H. Sun, M. Wang, M. Wang, L. Min, F. Cao, W. Tian, L. Li, *Adv. Mater.* **2022**, *34*, 2200221.
[25] J. Bao, M. G. Bawendi, *Nature* **2015**, *523*, 67.
[26] C. Zhou, O. J. F. Martin, E. Charbon, *Opt. Express* **2025**, *33*, 10475.
[27] M. Tian, B. Liu, Z. Lu, Y. Wang, Z. Zheng, J. Song, X. Zhong, F. Wang, *Light Sci Appl* **2024**, *13*, 278.
[28] A. Ahamed, A. Rawat, L. N. McPhillips, A. S. Mayet, M. S. Islam, *ACS Photonics* **2024**, *11*, 2497.
[29] Y. Zhang, S. Zhang, H. Wu, J. Wang, G. Lin, A. P. Zhang, *Nat. Commun.* **2024**, *15*, 3807.
[30] T. S. Moss, G. J. Burrell, B. Ellis, *Semiconductor Opto-Electronics*, Butterworth-Heinemann, Oxford, UK **1973**.
[31] M. A. Green, *Sol. Energy Mater. Sol. Cells* **2008**, *92*, 1305.
[32] W. Bai, J. Shin, R. Fu, I. Kandela, D. Lu, X. Ni, Y. Park, Z. Liu, T. Hang, D. Wu, Y. Liu, C. R. Haney, I. Stepien, Q. Yang, J. Zhao, K. R. Nandoliya, H. Zhang, X. Sheng, L. Yin, K. MacRenaris, A. Brikha, F. Aird, M. Pezhouh, J. Hornick, W. Zhou, J. A. Rogers, *Nat. Biomed. Eng.* **2019**, *3*, 644.
[33] D. Li, H. Jussila, L. Karvonen, G. Ye, H. Lipsanen, X. Chen, Z. Sun, *Sci. Rep.* **2015**, *5*, 15899.
[34] G. Li, Z. Ma, C. You, G. Huang, E. Song, R. Pan, H. Zhu, J. Xin, B. Xu, T. Lee, Z. An, Z. Di, Y. Mei, *Sci. Adv.* **2020**, *6*, aaz6511.
[35] E. Song, W. Si, R. Cao, P. Feng, I. Mönch, G. Huang, Z. Di, O. G. Schmidt, Y. Mei, *Nanotechnology* **2014**, *25*, 485201.
[36] L. Li, J. Niu, X. Shang, S. Chen, C. Lu, Y. Zhang, L. Shi, *ACS Appl. Mater. Interfaces* **2021**, *13*, 4364.
[37] M. A. Kats, D. Sharma, J. Lin, P. Genevet, R. Blanchard, Z. Yang, M. M. Qazilbash, D. N. Basov, S. Ramanathan, F. Capasso, *Appl. Phys. Lett.* **2012**, *101*, 221101.
[38] J. H. Jerman, D. J. Clift, S. R. Mallinson, *Sens. Actuators, A* **1991**, *29*, 151.
[39] W. Wang, X. Lu, X. Wu, Y. Zhang, R. Wang, D. Yang, X. Pi, *Adv. Mater. Interfaces* **2023**, *10*, 2202369.
[40] C. Gui, M. Elwenspoek, J. G. E. Gardeniers, P. V. Lambeck, *J. Electrochem. Soc.* **1998**, *145*, 2198.
[41] J. Henrie, S. Kellis, S. M. Schultz, A. Hawkins, *Opt. Express* **2004**, *12*, 1464.
[42] Z. Yang, Y. Chen, Y. Zhou, Y. Wang, P. Dai, X. Zhu, H. Duan, *Adv. Opt. Mater.* **2017**, *5*, 1700029.
[43] M. C. Gather, N. M. Kronenberg, K. Meerholz, *Adv. Mater.* **2010**, *22*, 4634.
[44] Q. Peng, Y. Guo, S. Liu, Z. Cui, *Opt. Lett.* **2002**, *27*, 1720.
[45] Z. Zheng, C. Liu, W. He, J. Huang, J. He, G. Huang, Y. Mei, C. Zheng, *Appl. Phys. Lett.* **2024**, *124*, 101903.
[46] B. Wu, Z. Zhang, Z. Zheng, T. Cai, C. You, C. Liu, X. Li, Y. Wang, J. Wang, H. Li, E. Song, J. Cui, G. Huang, Y. Mei, *Adv. Mater.* **2023**, *35*, 2306715.
[47] I. M. Ross, M. Kawazu, H. Sawada, A. Papworth, T. Walther, *J. Phys.: Conf. Ser.* **2011**, *371*, 012013.
[48] P. Zhang, E. Tevaarwerk, B.-N. Park, D. E. Savage, G. K. Celler, I. Knezevic, P. G. Evans, M. A. Eriksson, M. G. Lagally, *Nature* **2006**, *439*, 703.
[49] M. G. Lagally, S. Nanomembranes, *MRS Bull.* **2007**, *32*, 57.
[50] D. Yang, X. Ma, *Handbook of Integrated Circuit Industry*, Springer Nature, Singapore **2024**.
[51] A. Mannodi-Kanakkithodi, M. Y. Toriyama, F. G. Sen, M. J. Davis, R. F. Klie, M. K. Y. Chan, *npj Comput. Mater.* **2020**, *6*, 39.
[52] F. Wang, T. Zhang, R. Xie, Z. Wang, W. Hu, *Nat. Commun.* **2023**, *14*, 2224.
[53] D. Guo, Z. Wu, P. Li, Y. An, H. Liu, X. Guo, H. Yan, G. Wang, C. Sun, L. Li, W. Tang, *Opt. Mater. Express* **2014**, *4*, 1067.
[54] W. Demtröder, *Laser Spectroscopy: Basic Principles*, Vol. *1*, Springer, Berlin Heidelberg **2008**.
[55] C. Brown, A. Goncharov, Z. S. Ballard, M. Fordham, A. Clemens, Y. Qiu, Y. Rivenson, A. Ozcan, *ACS Nano* **2021**, *15*, 6305.
[56] E. Huang, Q. Ma, Z. Liu, *Sci. Rep.* **2017**, *7*, 40963.
[57] D.-W. Sun, H. Pu, J. Yu, *Nat. Rev. Electr. Eng* **2024**, *1*, 251.
[58] B. Lu, P. Dao, J. Liu, Y. He, J. Shang, *Remote Sens.* **2020**, *12*, 2659.
[59] P. Aggarwal, F. A. Papay, *Exp. Dermatol.* **2022**, *31*, 1128.
[60] X. Hadoux, F. Hui, J. K. H. Lim, C. L. Masters, A. Pébay, S. Chevalier, J. Ha, S. Loi, C. J. Fowler, C. Rowe, V. L. Villemagne, E. N. Taylor, C. Fluke, J.-P. Soucy, F. Lesage, J.-P. Sylvestre, P. Rosa-Neto, S. Mathotaarachchi, S. Gauthier, Z. S. Nasreddine, J. D. Arbour, M.-A. Rhéaume, S. Beaulieu, M. Dirani, C. T. O. Nguyen, B. V. Bui, R. Williamson, J. G. Crowston, P. van Wijngaarden, *Nat. Commun.* **2019**, *10*, 4227.